

FACILITY FORM 502

N66 21772	
49	1
CD-71406	12

N56-368

CONTINUUM FEEDBACK CONTROL OF A RAYLEIGH-TAYLOR TYPE INSTABILITY

by

James R. Melcher and Everett Paul Warren

Department of Electrical Engineering
Massachusetts Institute of Technology
Cambridge, Massachusetts

The electrohydrodynamics of a highly conducting interface stressed by a perpendicular electric field and attached (by surface tension) to a rigid circular wall are described in terms of a set of normal modes which satisfy four boundary conditions. The interface can be unstable either because of gravity (a heavy fluid on top of a light fluid) or because of the electric field. The experimental eigenfrequencies, eigenfunctions and conditions for instability are compared to the theory. These modes are then used to describe the dynamics when the interface displacement is detected and a proportionate potential is fed back to the segmented electrode which imposed the quiescent electric field. Electronic means for detecting interface disturbances are described together with the relationship between the sampling scheme and possible overstability. A comparison of theory and experiment is made for the eigenfrequencies with feedback, and conditions for significant improvement in stability are given.

GPO PRICE \$ _____

CFSTI PRICE(S) \$ _____

Hard copy (HC) \$ 2.00

Microfiche (MF) \$ 1.50

CONTINUUM FEEDBACK CONTROL OF A RAYLEIGH-TAYLOR TYPE INSTABILITY

by

James R. Melcher and Everett Paul Warren

Department of Electrical Engineering
Massachusetts Institute of Technology
Cambridge, Massachusetts

I. Introduction

The instability of the equilibrium formed when a heavy fluid is supported through hydrostatic pressure by a light fluid characterizes a variety of physical situations. Hence, this Rayleigh-Taylor type of instability appears in the literature of not only hydrodynamics⁽¹⁾, but in that of hydromagnetics⁽²⁾, plasma dynamics⁽³⁾ and electrohydrodynamics⁽⁴⁾ as well. In this work, the instability is often found to have disastrous effects. The obvious example is the instability of magnetic containment schemes. An analogous but even more severe problem exists with equilibria, which use electric fields to levitate, confine or orient liquids (which can be of arbitrary conductivity). This problem is the motivation for the work presented in the following sections, which first theoretically and experimentally explores the details of a potentially unstable electrohydrodynamic equilibrium, and then shows how external active circuits can be coupled to the continuum to provide a feedback, which stabilizes what would otherwise be an unstable situation. The case considered offers the opportunity to make a careful comparison of theory and experiment.

Fluids form a plane interface of radius R , as shown in Figure 1.

They are confined by rigid walls from above and below and at the radius R . The interface has a surface tension T , and is attached to the sharp edge of the wall at $r = R$. Now, if the density ρ_u of the upper fluid is greater than the density ρ_ℓ of the lower fluid, the top-heavy equilibrium may be unstable because of the gravitational acceleration g . The classic experiment of Duprez⁽⁵⁾ was devoted to determining the stabilizing effect of the attached interface. Both the continuity requirements of the rigid walls and the attached interface must be included to understand the effects of concern here.

It is assumed that the lower fluid is highly conducting (for example, water) while the upper fluid is insulating (air or oil). Then a potential difference is applied between the interface and the upper electrode. The resulting dynamics have been studied for the unbounded interface^(6,7,8), and with simple effects from boundaries⁽⁹⁾. The potential V tends to produce an unstable equilibrium. Hence, if the equilibrium is unstable to begin with, the addition of the potential only makes matters worse. However, an additional potential $v(r,\theta,t)$ may be applied over the surface of the electrode, and this potential made proportional to interface deflections. Then, an upward deflection of the interface is attended by a decrease, rather than an increase in the electric surface traction, and the electric field has the effect of stabilizing the equilibrium. In practice, it may in addition support the fluid.

The control of a continuum requires a feedback, which is dependent on both space and time. Practically, the interface deflections can only be spacially sampled, and a finite number of sensing signals used to approximate the potential $v(r,\theta,t)$.

This is the essential limitation on the use of feedback in stabilizing continua, and has been the subject of previous work relating to electromechanical instability,^(10,11) as well as to the control of chemical^(12,13) and nuclear⁽¹⁴⁾ reactors.

In Section II, a simple model is derived to account for effects from the boundary conditions and the electric field. The normal modes of the interface, with the electrode at a constant potential V are described in Section III, together with experiments concerning the eigenfrequencies, eigenmodes and conditions for instability. These modes are then used in Section IV to include the effect of a feedback derived by averaging the interface deflections over four sections of the surface and feeding back proportionate amplified signals to four segmented electrodes above the interface. The modal theory is easily adapted to other feedback schemes, while the experimental apparatus used to sense the deflections and produce the feedback signals meets the requirements for more practical situations.

II. Equation of Motion

The electromechanical interaction occurs only at the interface, and hence, we can write the bulk equations for the fluid as,

$$\rho \frac{\partial \bar{\mathbf{v}}}{\partial t} + \nabla p = -\rho g \bar{\mathbf{i}}_z \quad (1)$$

$$\nabla \cdot \bar{\mathbf{v}} = 0 \quad (2)$$

where $\bar{\mathbf{v}}$ and p are the fluid velocity and pressure respectively and g is the gravitational acceleration. We have dropped terms from Equation (1) not consistent with a linearized analysis.

The essence of the long-wave model is in the statements that the fluid velocities transverse to the z axis are independent of z and that the fluid acceleration in the z direction can be ignored to make the pressure essentially hydrostatic in its z dependence.

$$p = -\rho g z + \pi(r, \theta, t) \quad (3)$$

The conservation of mass condition (Equation 2) is then used to compute the z velocity. Solutions above and below the interface are distinguished by recognizing that in the upper fluid, $v_z^u(r, \theta, u, t) = 0$ while in the lower fluid $v_z^\ell(r, \theta, -\ell, t) = 0$. Hence,

$$v_z^u = -(z-u) \nabla \cdot \bar{\mathbf{v}}^u \quad (4)$$

$$v_z^\ell = -(z+\ell) \nabla \cdot \bar{\mathbf{v}}^\ell$$

where ∇ , $\bar{\mathbf{v}}^u$ and $\bar{\mathbf{v}}^\ell$ only depend on (r, θ, t)

The divergence of the difference between Equation (1) evaluated above and below the interface is

$$\frac{\partial}{\partial t} \nabla \cdot (\rho^u \mathbf{v}^u - \rho^\ell \mathbf{v}^\ell) + \nabla^2 (\pi^u - \pi^\ell) = 0 \quad (5)$$

This manipulation is performed because the difference $\pi^u - \pi^\ell$ is determined by the boundary condition that the interface be in force equilibrium, i.e.

$$\pi^u - \pi^\ell = g\xi(\rho^u - \rho^\ell) + T\nabla^2 \xi + \frac{1}{2} \frac{\epsilon V^2}{u^2} - \frac{\epsilon V \mathbf{v}}{u^2} + \frac{\epsilon V^2}{u^3} \xi \quad (6)$$

where T is the surface tension and ϵ is the permittivity of the upper fluid. Equation (6) requires that the difference between the fluid pressure above and below the interface is due to curvature effects from the surface tension and due to the electric traction.

The surface velocity $\partial \xi / \partial t = \mathbf{v}_z^u(z=0) = \mathbf{v}_z^\ell(z=0)$. Hence, substitution from Equations (4) into the first term of Equation (5), together with a substitution for $\pi^u - \pi^\ell$ (given by Equation (6)) in the second term of Equation (5) gives

$$\eta \frac{\partial^2 \xi}{\partial t^2} + \nabla^4 \xi - G \nabla^2 \xi - \frac{\epsilon V}{u^2 T} \nabla^2 \mathbf{v} = 0 \quad (7)$$

where we have defined the parameters,

$$\eta = \left(\frac{\rho^u}{u} + \frac{\rho^\ell}{\ell} \right) / T$$

$$G = g \left(\frac{\rho^\ell}{T} - \frac{\rho^u}{T} \right) - \frac{\epsilon V^2}{u^3 T}$$

This is the required equation of motion. If the potential v on the upper electrode is independent of space and time, Equation (7) provides a description of the long-wave motions of the interface, with the effects of gravity and quiescent electric field (G), as well as surface tension, included. Feedback to the upper electrode will be a rather complicated function of the surface deflection ξ . To understand motions of the interface in the presence of feedback, it is first necessary to form a complete picture of the "open loop" dynamics. Hence, Section III is devoted to the electrohydrodynamics without feedback, and the results of that section are then used in Section IV where the feedback problem is undertaken.

III. Electrohydrodynamics Without Feedback

A. Eigenmodes

There is little work in the classical literature that considers the dynamics of fluids with free surfaces confined in three dimensions with the effect of surface tension included. Experiments, such as that of Duprez⁽⁵⁾, that demonstrate the effect of boundaries on the conditions for impending Rayleigh-Taylor instability, intrinsically depend on the "static" nature of the instability. That is, the analysis assumes that instability does not depend on inertial effects, and experiments as well as theories, which ignore the transverse boundaries support this conjecture. As will be shown here, this is fortuitous, in that such a procedure ignores a class of modes which can be unstable. Moreover, dynamical effects are extremely important if the eigenmodes are to be understood under any conditions other than those for impending instability. In the presence of an active boundary, the system is likely to be overstable, and dynamical considerations are essential.

The ordinary gravity-wave resonator can be understood by simply superimposing solutions which are periodic in space, to satisfy boundary conditions. This is an adequate procedure when there is only one pair of boundary conditions to be satisfied. Additional boundary conditions arise when a fluid resonator has sufficiently small dimensions to make the effect of surface tension significant. In the experiments described here, the surface tension fixes the surface at $r = R$, where a rigid wall also requires that the radial velocity be zero. It is this second condition which can be ignored for some modes at the point of impending instability, if the principle of exchange of stabilities holds. Here, this principle is not appropriate, and hence one boundary condition is

$$\left[\xi \right]_{r=R} = 0 \quad (8)$$

while, from the radial component of Equation (5) (before the divergence is taken) and from Equation (6), the condition that $v_r(r = R) = 0$ can be written

$$\frac{\partial}{\partial r} \left[(\nabla^2 - G) \xi - \frac{\epsilon V}{Tu^2} v \right]_{r=R} = 0 \quad (9)$$

With $G = 0$ and $v = 0$, Equation (7) has the same form as found in analyzing transverse vibrations of a thin plate.⁽¹⁵⁾ The second order term introduced with G complicates matters somewhat, but more important, boundary conditions (8) and (9) do not lead to modes which satisfy the usual orthogonality conditions.

Solutions have the form $\xi = \text{Re } \hat{\xi}(r) \exp j(\omega t - m\theta)$, where it follows from Equation (7) that (for $v = 0$),

$$(\nabla^2 - \alpha^2) (\nabla^2 + \beta^2) \hat{\xi}(r) = 0 \quad (10)$$

$$(\nabla^2 \equiv \frac{1}{r} D r D - \frac{m^2}{r^2}) ; \quad D \equiv \frac{\partial}{\partial r}$$

with α and β related to the frequency ω by

$$\begin{aligned} \alpha^2 &= (G + \sqrt{G^2 + 4\omega^2 \eta})/2 \\ \beta^2 &= (-G + \sqrt{G^2 + 4\omega^2 \eta})/2 \end{aligned} \quad (11)$$

Hence, the four solutions are a superposition of the pairs of solutions provided by the Bessel's equations in brackets (Equation 10). One of each of these pairs of solutions is singular at the origin, and hence the required solution is

$$\hat{\xi}_{mn} = \frac{J_m(j\alpha_{mn} r)}{J_m(j\alpha_{mn} R)} - \frac{J_m(\beta_{mn} r)}{J_m(\beta_{mn} R)} \quad (12)$$

where the linear combination is taken to satisfy Equation (8). To satisfy the condition of Equation (9) (with $v = 0$), α and β are related by the eigenvalue equation

$$(j\alpha_{mn} R) \frac{J'_m(j\alpha_{mn} R)}{J_m(j\alpha_{mn} R)} = (\beta_{mn} R) \frac{J'_m(\beta_{mn} R)}{J_m(\beta_{mn} R)} \quad (13)$$

which has been simplified by using Equations (10) and (11).

Equation (11) shows that in addition α_{mn} and β_{mn} are related by

$$(\alpha_{mn} R)^2 = GR^2 + (\beta_{mn} R)^2 \quad (14)$$

Equations (13) and (14) may be solved for the eigenvalues β_{mn} , and a normalized eigenfrequency squared $\Omega^2 = \omega^2 \eta R^4$ is then given by

$$\Omega_{mn}^2 = (\beta_{mn} R)^2 \left[(\beta_{mn} R)^2 + GR^2 \right] \quad (15)$$

These eigenfrequencies (m,n) are shown as a function of GR^2 in Figure 2. The lowest radial mode is given when $n = 1$. The parameter GR^2 can be varied by changing the quiescent electric

field V/u . For example, with the heavier fluid below the interface and no electric field, GR^2 will be positive. Then raising the electric field reduces GR^2 , and from Figure 2, reduces each of the eigenfrequencies. Eventually, each of the eigenfrequencies squared becomes negative, and the mode becomes unstable. The (1,1) mode is the first to become unstable.

Physically, large positive values of GR^2 imply that the effect of the gravitational field on the dynamics is much greater than that of the surface tension. In the limit where $GR^2 \rightarrow \infty$, $\alpha R \rightarrow \infty$ and Equation (13) reduces to $J'_m(\beta_{mn} R) = 0$. Except in a region very near the edge ($r = R$), the eigenfunctions are essentially Bessel's functions of real argument, with zero slope at $r = R$. This is the situation of a gravity wave resonator⁽¹⁶⁾ with a surface tension "boundary layer" near the walls. The (1,1) eigenmode is shown in Figure 3. As GR^2 is reduced, the point of zero slope on the lowest eigenfunction (shown in Figure 3), moves inward from the resonator boundaries but remains skewed somewhat to the outside of the half-radius. Instability impends when GR^2 is sufficiently negative to make $\omega = 0$, or when $(\alpha R)^2 \rightarrow 0$ and $(\beta R)^2 \rightarrow GR^2$ (Equations 11). Then Equation (13) (for modes $m \neq 0$) reduces to $J_m(\beta_{mn} R) = 0$ and the eigenfunctions are Bessel's functions having zeros at $r = R$. The cases where $GR^2 \rightarrow \infty$, $GR^2 > 0$ and $GR^2 < 0$ (impending instability) are compared in Figure 3.

The $m = 0$ modes differ from the others because they do not automatically satisfy the condition that the total mass within the resonator be conserved. At low values of GR^2 (even the point of impending instability) both boundary conditions influence the modes. This accounts for the peculiar appearance of the $m = 0$ eigenfrequency shown in Figure 2.

In the extreme of large GR^2 , the boundary condition imposed by the rigid wall at $r = R$ on the radial velocity is essential, with the effect of the attached interface insignificant. By contrast, at the point of impending instability the attached interface imposes the significant condition and the rigid wall at $r = R$ is unimportant, unless $m = 0$. This is why only the former boundary condition need be considered in predicting the usual forms of Rayleigh-Taylor instability (where the principle of exchange of stabilities is valid), so long as the first mode to become unstable happens to be with $m \neq 0$.

The modes described here will be used in Section IV to expand the potential $v(r, \theta, t)$. There it will be convenient to use modes $v_{mn}(r)$, defined so that

$$R^2 \nabla^2 \hat{v}_{mn} = \hat{\xi}_{mn} \quad (16)$$

It follows from Equation (10) that

$$\nabla^4 \hat{v}_{mn} - G \nabla^2 \hat{v}_{mn} = \omega_{mn}^2 \eta \hat{v}_{mn} \quad (17)$$

where, from Equation (16)

$$\left[\nabla^2 \hat{v}_{mn} \right]_{r=R} = 0 \quad (18)$$

The second boundary condition follows from Equations (9), (16), and (17), since

$$D(\nabla^2 - G) \nabla^2 \hat{v}_{mn} = \omega_{mn}^2 \eta D \hat{v}_{mn} = 0 \quad (19)$$

or

$$\left[D\hat{v}_{mn} \right]_{r=R} = 0 \quad (20)$$

This boundary condition also insures that the functions $\hat{\xi}_{mn}$ satisfy the boundary condition (9) even when $v = v(r, \theta, t)$, so long as v is represented by a summation of the modes \hat{v}_{mn} .

In the appendix, it is shown that these modes \hat{v}_{mn} satisfy the orthogonality condition.

$$\int_0^R r (D\hat{v}_{mn} D\hat{v}_{mp} + \frac{m^2 \hat{v}_{mn} \hat{v}_{mp}}{2r}) dr = 0, \quad n \neq p \quad (21)$$

which is more complicated than usual because the boundary conditions do not appear in the usual convenient combination. (17)

B. Experiments

Before introducing the complication of feedback, the physical significance of the electrohydrodynamic model is explored experimentally. The long-wave model depends for its validity on there being surface deflections with "wave-lengths" long compared to the depths l and u . For this reason, the eigenmodes become more and more subject to question as the mode numbers are increased. Fortunately, it is the lowest mode (1,1) which is most critical in terms of instability, and hence, is of most concern.

The eigenfrequency Ω_{11} appears as the lowest resonant frequency, when the fluid resonator is subjected to vibrations in the plane of the interface. In this experiment, the surface deflections are measured with a capacitance probe positioned just above the interface. The probe uses a 72 mc/sec tuned circuit in the same way as will be described for feedback sensing purposes in the

next section. However, here the probe surface is circular and is of radius $0.16R$. This makes it possible to both vary the vibration frequency to find the maximum deflection frequencies (eigenfrequencies), and to measure the spacial dependence of the individual modes.

The eigenfrequency of the lowest mode is shown as a function of GR^2 in Figure 4. Here, the voltage was raised to decrease GR^2 and the resulting data can be compared to the plot of theoretical frequencies (predicted in Section IIIA). As expected, the higher eigenfrequencies are predicted with increasing inaccuracy. Experimental and theoretical eigenfrequencies are compared (with no applied voltage) in Table I for the resonator used to obtain the frequency shifts of Figure 4.

The capacitance probe makes it possible to map the interface deflections and identify the eigenmodes. The radial variation of the (1,1) mode is compared to the theoretical eigenmode in Figure 5. The probe measures a deflection averaged over the relative length shown in this figure.

The conditions for instability have been measured for the infinite interface.^(6,7,8) The effect of the boundaries can be included at the point of impending instability without recourse to the long-wave model, if (as pointed out in Section IIIA) the interface is assumed to attach to the edges and those modes which are affected by conservation of mass are ignored. For example, a square resonator will be unstable for V larger than⁽⁹⁾

$$V = \sqrt{\frac{uT}{\epsilon} \left[(ku)^2 + \left(\frac{\rho g u^2}{T} \right) \right]} / (ku) \coth(ku) \quad (22)$$

where k is allowed to be

$$k = \pi \sqrt{n^2 + m^2/L^2}, n = 1,2,3,\dots, m = 2,4,6,\dots \quad (23)$$

and has that value in Equation (22) which gives the least voltage V for instability.

The voltage for instability, as a function of interface-electrode spacing u, is shown in Figure 6. Here, the liquid is water, and sulfurhexafluoride (a gas) is used to prevent electrical breakdown. It is clear from the data and the theoretical curves predicted by Equation (22) that the boundaries have a significant effect of the conditions for instability.

IV. Electrohydrodynamics With Feedback

The potential $v(r, \theta, t)$ is now used to produce a stabilizing feedback force on the interface. The experiment is as shown in Figure 7, where the upper electrode is shown segmented into four equi-area pies. Each pie is connected to a feedback loop, as shown. The capacitance between a given electrode and the interface is part of a tank circuit isolated by a capacitor and tuned near resonance for a 72 Mc/sec driving signal. Hence, the spacial average (over one pie) of the interface deflection shifts the resonant frequency, with a proportionate change in the operating point of the tube. As a result, a demodulated signal proportional to the average deflection of the interface appears across the cathode resistor. This signal is amplified (to $10^5 - 10^7$ V/m) and fed back through a low pass filter to the segment which originated the signal. Each segment has a separate feedback loop, with the carrier frequencies for the sensing circuits differing by about 1 Mc/sec to insure isolation between loops.

The eigenmodes developed in Section IIIA, and experimentally studied in Section IIIB, are coupled by the feedback, with a resulting shift in the eigenfrequencies. The new eigenmodes, with coupling to the active boundary at $z = u$, will be approximated by

$$\xi = \text{Re} \sum_{m=0}^{\infty} \sum_{n=1}^{\infty} \hat{\xi}_{mn}(r) \left(\frac{V_{mn}^o}{V_{mn}^e} \sin m\theta + \frac{V_{mn}^e}{V_{mn}^o} \cos m\theta \right) e^{j\omega t} \quad (24)$$

where $\hat{\xi}_{mn}(r)$ is given by Equation (12).

Since each term in the expansion of the coupled eigenmode must satisfy Equation (7) and the boundary conditions of Equations (8) and (9), the electrode potential is expanded as

$$v = \text{Re} \sum_{m=0}^{\infty} \sum_{n=1}^{\infty} \hat{v}_{mn}(r) \left(V_{mn}^o \sin m\theta + V_{mn}^e \cos m\theta \right) e^{j\omega t} \quad (25)$$

where the modes \hat{v}_{mn} are related to $\hat{\xi}_{mn}$ by Equation (16) and are

$$\hat{v}_{mn} = \frac{J_m(j\alpha_{mn} r)}{(R\alpha_{mn})^2 J_m(j\alpha_{mn} R)} + \frac{J_m(\beta_{mn} r)}{(R\beta_{mn})^2 J_m(\beta_{mn} R)} \quad (26)$$

as can be verified by using the differential equations (10) satisfied by $J_m(j\alpha_{mn} r)$ and $J_m(\beta_{mn} r)$. The modes \hat{v}_{mn} are orthogonal in the sense of Equation (21), and because they satisfy Equation (20), they may be used to expand $v(r, \theta, t)$ without violating Equation (9)

as a boundary condition on the modes $\hat{\xi}_{mn}$.

Because the feedback voltage on the i 'th electrode is proportional to the spacial average of the surface deflection below the i 'th electrode,

$$v_i(t) = \frac{4A}{\pi R^2} \int_0^R \int_{(i-1)\pi/2}^{i\pi/2} \xi r dr d\theta \quad (27)$$

Here, it is assumed that there are four electrode segments, arranged as shown in Figure 8, with $\theta = 0$ between two of the segments. The average deflection is amplified by the gain A , which will be taken as independent of frequency.

The substitution of ξ (Equation(24)), into Equation (27) gives

$$v_i(t) = \text{Re} \hat{v}_i e^{j\omega t} \quad (28)$$

where

$$\begin{aligned} \hat{v}_i = & \frac{4A}{\pi} \sum_{m=0}^{\infty} \sum_{n=1}^{\infty} \frac{a_{mn}}{m} \left\{ \frac{0}{mn} \left[\cos \frac{m\pi(i-1)}{2} - \cos \frac{m\pi i}{2} \right] \right. \\ & \left. + \frac{e}{mn} \left[\sin \frac{m\pi i}{2} - \sin \frac{m\pi(i-1)}{2} \right] \right\} \end{aligned}$$

and ($x = r/R$)

$$a_{mn} = \int_0^1 x \hat{\xi}_{mn}(x) dx$$

These electrode potentials determine the potential amplitudes V_{mn}^0

and V_{mn}^e of Equation (25) in terms of the deflection amplitudes \overline{v}_{mn} . Here, the integral condition of Equation (21) is useful.

That is, if Equation (25) is operated on first by $\left(\frac{\sin p\theta}{\cos p\theta} \right) (D\hat{v}_{ps}) r D$ and then by $r \left(\frac{\sin p\theta}{\cos p\theta} \right) \hat{v}_{ps} \frac{m}{r^2}$ and the sum is taken of the resulting equations, followed by an integration over the electrode surface, the orthogonality condition of Equation (21) reduces the resulting expression to,

$$\begin{bmatrix} V_{ps}^o \\ V_{ps}^e \end{bmatrix} = \frac{f_{ps}}{\pi b_{ps}} \sum_{i=1}^4 \frac{\hat{v}_i}{P} \begin{bmatrix} \cos \frac{p(i-1)\pi}{2} - \cos \frac{pi\pi}{2} \\ \sin \frac{pi\pi}{2} - \sin \frac{p(i-1)\pi}{2} \end{bmatrix} \quad (29)$$

where $(x = r/R)$

$$b_{ps} = \int_0^1 x \left\{ \left[D\hat{v}_{ps}(x) \right]^2 + \frac{p^2}{x^2} \left[\hat{v}_{ps}(x) \right]^2 \right\} dx$$

$$f_{ps} = \int_0^1 \frac{p^2}{x} \hat{v}_{ps}(x) dx$$

Now, the v_i 's have been found as a function of the amplitudes \overline{v}_{mn} (Equation (28)) and hence, Equation (29) shows the effect of the deflection modes on the electrode potential modes. The equation of motion (Equation 7) provides the inverse effect of the electrode modes on the deflection modes. Substitution of Equations (24) and (25) into Equation (7) shows that

$$\begin{aligned} (\Omega_{mn}^2 - \Omega^2) \begin{bmatrix} \text{---}^o \\ \text{---}_{mn} \end{bmatrix} &= \frac{\epsilon VR^2}{u^2 T} \begin{bmatrix} v_{mn}^o \\ v_{mn}^e \end{bmatrix} \\ \begin{bmatrix} \text{---}^e \\ \text{---}_{mn} \end{bmatrix} & \end{aligned} \quad (30)$$

where the Ω_{mn} 's are the eigenfrequencies without feedback (Section III) and Ω is the eigenfrequency with feedback. With feedback, Equations (30) and (29) (written using \hat{v}_i from Equation (28)) must be simultaneously satisfied. Hence, substitution for v_{mn}^o and v_{mn}^e in Equation (30) gives

$$\begin{bmatrix} \text{---}^o \\ \text{---}_{mn} \\ \text{---}^e \\ \text{---}_{mn} \end{bmatrix} (\Omega_{mn}^2 - \Omega^2) - \frac{M f_{mn}}{m \pi^2 b_{mn}} \sum_{p=0}^{\infty} \sum_{q=1}^{\infty} \frac{a_{pq}}{p} \begin{bmatrix} \text{---}^o & \sigma_{mp} \\ \text{---}_{pq} & \epsilon_{mp} \\ \text{---}^e & \\ \text{---}_{pq} & \end{bmatrix} = 0 \quad (31)$$

where

$$M = \frac{4 \epsilon VAR^2}{u^2 T}$$

$$\Omega^2 = \omega^2 R^4 \eta$$

$$\sigma_{mp} = \sum_{i=1}^4 \left[\cos \frac{m(i-1)\pi}{2} - \cos \frac{mi\pi}{2} \right] \left[\cos \frac{p\pi(i-1)}{2} - \cos \frac{p\pi i}{2} \right]$$

$$\epsilon_{mp} = \sum_{i=1}^4 \left[\sin \frac{im\pi}{2} - \sin \frac{m(i-1)\pi}{2} \right] \left[\sin \frac{ip\pi}{2} - \sin \frac{p\pi(i-1)}{2} \right]$$

It is clear from Equation 31 that in the absence of feedback ($M = 0$) the amplitudes \overline{a}_{mn} individually represent solutions having frequencies $\Omega = \Omega_{mn}$ but that with feedback these amplitudes are coupled and the frequencies are therefore changed. To calculate the coupled frequencies, the surface deflections are approximated by a finite number of amplitudes i.e. $p = 0, 1, 2, \dots, i$, $q = 1, 2, 3, \dots, j$. Then Equation (31) can be written for $m = 0, 1, \dots, i$, $n = 1, 2, \dots, j$ and this gives jxi equations which are homogeneous in the \overline{a}_{mn} 's. The compatibility of these equations is a polynomial in Ω^2 , and hence can be solved for the eigenfrequencies.

Most of the spacial variation introduced by the feedback occurs in the azimuthal direction, so that more azimuthal than radial modes are required to adequately describe the dynamics. (19) In the work which follows, the first six (odd and even) azimuthal modes and the first two radial modes are considered. For the four segment situation considered here, the $m = 0$ mode is not revised by the feedback ($a_{on} = 0$) and therefore, only the $n = 1$ radial modes are involved in the coupling.

The eigenfrequencies are shown in Figure 9, as a function of GR^2 , in the case where the feedback gain A is such that $M = 10^3$. These frequencies can be compared to those shown in Figure 2, where the feedback gain $A = 0$. As already observed the (0,1) mode remains unaffected. The essential consequence of the feedback is an increase in the frequency of the (1,1) mode, so that the point of impending instability (as the voltage is raised so that GR^2 is made more negative) is determined by the (0,1) mode rather than the (1,1) mode. At lesser values of M , the value of GR^2 where $\Omega \rightarrow 0$ is shifted to the left, but not so far as shown in Figure 9. Hence, the conditions for stability of all modes can be represented as shown in Figure 10. At low values of the gain M , instability first occurs in the coupled (1,1) and (1,3) modes. In this case the voltage for instability can be increased (GR^2 decreased) by increasing the gain. Finally, the (0,1) mode is the first to become unstable and there is no advantage in further increasing the gain.

In the range where the (1,1) mode is the first to become unstable, without feedback, a theory based on the coupling of the (1,1) and (1,3) modes gives the line of marginal stability (shown in Figure 10) as

$$M = - \Omega_{11}^2 \Omega_{31}^2 / (\Omega_{11}^2 H_{33} + \Omega_{31}^2 H_{11})$$

(32)

where $\Omega_{\alpha\beta}$ is the eigenfrequency of the (α,β) mode without feedback and $H_{\alpha\beta} = -4f_{\alpha 1} a_{\beta 1} / \alpha_{\beta} \pi^2 b_{\alpha 1}$.

Overstability has been found both experimentally and theoretically in situations similar to the one described here.⁽¹⁰⁾ However, the investigations described in this section did not uncover an overstable situation: apparently a result of using an average of the surface deflection (Equation 27) to derive the feedback signal. By contrast, the deflections could be sampled at discrete positions to provide the sensing signals v_i . Although this can be advantageous in dealing with static instability (one has the liberty of choosing the sampling point within a given area) it has proved to be the cause of overstability in previous work.^(10,11)

Probably, there would be some increase in the stable region of Figure 9 if the feedback (still using four stations) incorporated one circular electrode at the center and three equi-area segments around the periphery. However, the intent here is to demonstrate the basic considerations involved, and not to optimize the system.

B. The Experiment With Feedback

The feedback is introduced to alter the natural frequencies of the fluid interface. In the absence of viscous effects, and with the type of feedback used here, these frequencies are either real, or purely imaginary. Hence, in the stable regime, a sinusoidal vibration of the resonator gives a response on the feedback loops with resonances at the eigenfrequencies. This is a convenient way to determine the effect of the feedback. With the voltage $V = 0$, the loop gains are adjusted to some gain A . Then, the resonance frequency of a given mode (the natural frequency) is

followed as the voltage is increased. This makes it possible to compare theory and experiment through the correlation of frequency shifts as a function of the applied voltage V . Data taken by measuring the (1,1) resonance as a function of applied voltage V are shown in Figure 11. With no gain ($A = 0$) the frequency squared decreases monotonically toward zero, where instability impends. With a feedback gain $A = A'$ the frequency first increases, and then decreases as the destabilizing effect of the voltage (proportional to V^2) overtakes the stabilizing effect of the feedback (proportional to V). With $A = 2A'$, the increase in frequency is still larger, but the peak still occurs at essentially the same voltage. The solid curves shown in Figure 11 are predicted using a gain $A' = 2.05 \times 10^6$ volts/meter. All of the theoretical curves have been displaced downward by $f^2 = 1.7$ to suppress the (8%) constant error in the predicted natural frequency (apparent in Figure 4). The closed loop measurement of frequency shift has been found to be the most practical technique for establishing the effective gain A . (In the experiment, there were four loops, each having three d-c amplifiers, an r-f oscillator and two r-f amplifiers so that establishing equal constant gains in each loop was difficult.)

An "open-loop" measurement of the high-voltage amplifier response to a known electrode potential distribution also provides a direct measurement of the gain A . That is, a perturbation potential v_d on electrodes (1) and (4) in Figure (8), with no perturbation potential on electrodes (2) and (3) establishes (from Equation (29)) that

$$v_{ps}^0 = 0$$

(33)

$$v_{ps}^e = \frac{f_{ps} v_d}{\pi b_{ps} p} \left(\sin \frac{p\pi}{2} - \sin \frac{3p\pi}{2} \right) \quad (34)$$

Here, the low frequency feedback from the high voltage amplifier has been disconnected. Hence, Equation (30) can be used directly to compute the resulting deflection amplitudes.

$$\frac{0}{-} = 0 \quad (35)$$

$$\frac{e}{-} = \epsilon VR^2 V_{mn}^e / u^2 T \Omega_{mn}^2 \quad (36)$$

Of course, it is assumed that the resulting deflections are static so that $\Omega^2 = 0$, and this means that the measurement is taken with GR^2 sufficiently large to insure stability. The response of the high voltage amplifier to this deflection is Equation (28), which by virtue of Equations (34) and (36) shows that

$$A = (v_i)_{\text{response}} / v_d C_i \quad (37)$$

where

$$C_i = \frac{4\epsilon VR^2}{\pi u^2 T} \sum_{m=0}^{\infty} \sum_{n=1}^{\infty} \frac{a_{mn} f_{mn}}{(\Omega_{mn})^2 b_{mn}} \left(\sin \frac{m\pi}{2} - \sin \frac{3m\pi}{2} \right) \left(\sin \frac{im\pi}{2} - \sin \frac{(i-1)m\pi}{2} \right)$$

Measurement of the gain, using open loop measurements of v_i and computed calibration constants C_i , resulted in a value of A'

about 15% higher than used for the theoretical curves of Figure 11. This is well within the experimental errors involved in the "open-loop" measurements, but is a significant error when viewed in terms of the "closed-loop" measurements.

V. Summary and Conclusions

The objective of this work has been to demonstrate the control of a fluid instability by coupling to an active electronic network. There are two essential considerations in this approach to the stability problem. First a means must be provided to sense the appropriate motions of the fluid without interfering with the equilibrium "flow." Signals derived from this sensing signal (which is in general both a function of space and time) must in turn be used to force the fluid motions, and this means that an externally controlled fluid force must be available. In the work undertaken here a solution to each of these problems has been illustrated, using as an example the stabilization of the Rayleigh-Taylor type surface instability. Radio-frequency capacitance probes were used to sense motions of the interface with a negligible influence on the motions themselves. An electric field then provided a natural means of feeding back a forcing function to the interface in proportion to the sensing signal.

Sections II and III were devoted to establishing a relatively simple but meaningful quasi-two-dimensional model for the field-coupled surface instability. Since the effect of the feedback was pictured in terms of a coupling between the normal modes without feedback, it was necessary to include the effects of radial boundary conditions. This made it possible to correlate theory with

experiments which demonstrated the eigenmode shape, the effect of an equilibrium electric field on the most critical eigenfrequency, and the effect on conditions for instability of boundaries which both confined the fluid and constrained the motions of the interface. Section IV then demonstrated how these eigenmodes were coupled by the feedback to increase the stable regime. The theoretical dependence of the most critical eigenfrequency on the feedback gain was finally shown experimentally. Emphasis has been placed on the behaviour of the eigenmodes rather than the regime of stability. In fact, from Figure 10

$$\Delta^2 = \frac{[g(\rho^\ell - \rho^u)R^2/T] + 26}{[g(\rho^\ell - \rho^u)R^2T] + 14.5} \quad (38)$$

where Δ is the ratio of the largest V consistent with stability with feedback to the largest possible V consistent with stability without feedback. That is Δ^2 is the largest possible factor of improvement in the electric pressure consistent with stability. For the air-water resonator having the dimensions used in this work, $g(\rho^\ell - \rho^u)R^2/T = 49.1$ and $\Delta^2 = 1.18$. Either a smaller resonator or a two liquid system would be required to demonstrate a larger improvement in the electric pressure.

In a practical situation, the equilibrium electric field can be used to levitate or orient an isolated volume of fluid, with the feedback used to insure stability. The essence of the sensing and driving schemes described here are directly applicable to this problem, and it is in this context that work on the regime for stability will be reported.

This work has considered the feedback control of an absolute instability. Closely related work concerning the use of similar techniques to control a convective instability (or amplifying wave) will be reported elsewhere.

Acknowledgments

This work was supported under NASA Research Grant NsG-368.

Appendix

To show that modes which satisfy Equation (17) and boundary conditions (18) and (20) are orthogonal in the sense of Equation (21), Equation (17) is used to write

$$\begin{aligned} \eta_{mn}^2 \int_0^R \left(Dv_{mn} Dv_{mp} + \frac{m^2}{r^2} v_{mn} v_{mp} \right) dr &\equiv \psi_{mnp} \\ &= \int_0^R \left[D(\nabla^4 v_{mn} - G\nabla^2 v_{mn}) r Dv_{mp} + \frac{m^2}{r} (\nabla^4 v_{mn} - G\nabla^2 v_{mn}) v_{mp} \right] dr \end{aligned}$$

Integrating the first term on the right by parts and recombining the remaining integrand gives,

$$\psi_{mnp} = \left[r(\nabla^4 v_{mn} - G\nabla^2 v_{mn}) Dv_{mp} \right]_0^R - \int_0^R \left(\nabla^4 v_{mn} \nabla^2 v_{mp} - G\nabla^2 v_{mn} \nabla^2 v_{mp} \right) dr$$

The first term is zero because of Equation (20), while the first term in the integrand can be expanded and partly integrated by parts to obtain,

$$\begin{aligned} \psi_{mnp} &= - \left[r(D\nabla^2 v_{mn}) \nabla^2 v_{mp} \right]_0^R \\ &+ \int_0^R \left[D\nabla^2 v_{mn} D\nabla^2 v_{mp} + \left(\frac{m^2}{r^2} + G \right) \nabla^2 v_{mn} \nabla^2 v_{mp} \right] dr \end{aligned}$$

Appendix

Again the first term vanishes by virtue of Equation (18). Then, the difference $\psi_{mnp} - \psi_{mpn}$ is zero (the remaining integrals are symmetrical in n and p) and the desired orthogonality condition (Equation 21) follows for $\omega_{mn} \neq \omega_{mp}$.

TABLES

Table I. Comparison of theoretical and experimental eigenfrequencies of higher order modes showing the increasing disparity arising from the failure of the long-wave model. Data for the resonator are given in Figure 4.

(m,n)	f_{mn} (cps) theoretical	f_{mn} (cps) experimental
1,1	3.36	3.10
0,1	7.57	6.40
1,2	11.1	9.1
0,2	16.5	12.9
1,3	24.0	15.0

REFERENCES

1. H. Lamb, Hydrodynamics (Dover Publications, New York, 1945.)
6th edition, p. 461.
2. S. Chandrasekhar, Hydrodynamic and Hydromagnetic Stability
(Oxford Press, London, 1961) p. 90.
3. T. H. Stix, The Theory of Plasma Waves, (McGraw-Hill Book Company, Inc. New York, 1962), p. 79.
4. J. R. Melcher, Field-Coupled Surface Waves, (M.I.T. Press, Cambridge, Massachusetts, 1963), p. 39.
5. A Summary of Deprez's work (1851) is given in, Encyclopedia Britannica, Vol. V (Samuel L. Hall, New York, 1878) 9th edition p. 69.
6. J. R. Melcher, "Electrohydrodynamic and Magnetohydrodynamic Surface Waves and Instabilities", Phys. of Fluids, 4, 11(1961) p. 1348.
7. J. R. Melcher, Field-Coupled Surface Waves (M.I.T. Press, Cambridge, Massachusetts, 1963), p. 61.
8. G. I. Taylor and A. D. McEwan, Journal of Fluid Mech. 22, part 1, p. 1 (1965).
9. J. R. Melcher, Phys. of Fluids, 5, 9 (1962) p. 1130.
10. J. R. Melcher, Proc. of IEEE, 53, 5 (1965) p. 460.
11. J. R. Melcher, IEEE Trans. on Aut. Cont. AC-10, 4 (1965)p. 466.
12. M. Murray "Model Analysis of Linear Distributed Control Systems", Ph.D. Dissertation, Department of Electrical Engineering M.I.T., (1965).
13. M. Gordon-Clark, "Dynamic Models for Convective Systems", Ph.D. Dissertation, Department of Electrical Engineering, M.I.T. (1966)

REFERENCES

14. D. M. Wiberg, "Optimal Feedback Control of Spatial Zenon Oscillations in a Nuclear Reactor, Ph.D. dissertation, C.I.T., (1965).
15. J. W. S. B. Rayleigh, The Theory of Sound (Dover Publications New York, 1945) Vol. 1 p. 359.
16. H. Lamb, op. cit. p. 364.
17. S. Chandrasekhar, op. cit. p. 637.
18. J. R. Melcher, Field-Coupled Surface Waves, (M.I.T. Press, Cambridge, Massachusetts, 1963), p. 62.
19. An indication of the number of modes required (as a function of the number of feedback electrodes) to predict possible types of instability for a somewhat similar system is given in Reference 10.

FIGURE CAPTIONS

Figure 1. Cross-sectional and top view of electrohydrodynamic resonator. The interface between two liquids is attached at $r = R$ to a rigid wall. The lower liquid is highly conducting and bounded from below by a rigid highly conducting plate, while the upper liquid is insulating and bounded by a rigid surface at the potential $v(r, \theta, t) = V$.

Figure 2. Eigenfrequencies in the absence of feedback for the modes (m, n) . Raising the potential V leads to a decrease in GR^2 which reduces all of the frequencies to the point where they become imaginary and instability impends.

Figure 3. The surface deflection in the $(1, 1)$ mode. When GR^2 is very large the eigenfunction approaches that of an ordinary gravity wave. At the point of impending instability ($GR^2 \rightarrow 0$) inertial effects are unimportant and the mode peaks at about a half radius. For an air-water interface and a radius R of about 2 cm, GR^2 is about 50, and the deflections peak midway between the half radius and the outer boundary.

Figure 4. Experimentally measured eigenfrequencies (\circ) as a function of GR^2 (varied by changing the applied voltage V). The solid line is the theoretical result of Section IIIA, $R = 1.9\text{cm}$, $u = 0.785\text{ mm}$, $\ell = 3\text{ mm}$ and the fluids are water and air.

Figure 5. Comparison of theoretical and experimental $(1, 1)$ mode eigenfunctions. The experimentally determined deflections represent averages over approximately the probe area. The relative size of the probe is shown.

Figure 6. Voltage V for instability as a function of the electrode interface spacing u . The resonator is square, and the three theore-

FIGURE CAPTIONS

tical curves are predicted by Equation (22).

Figure 7. Fluid surface coupled to feedback structure composed of four segments. The sensing and driving circuit for one of the segments is shown.

Figure 8. Top view of electrode at $z = u$, showing the four segments with connections to the four feedback loops.

Figure 9. Lowest eigenfrequencies with feedback. Here, $M = 10^3$ which characterizes the magnitude of the feedback gain used in experiments described in Section IVB. The curves are based on the coupling of two modes, and differ very little from those predicted using the coupling of three modes; (1,1), (3,1) and (5,1).

Figure 10. Regime of stability as a function of the feedback M . For small values of M there is an improvement in the electric pressure consistent with stability. Eventually, modes that are unaffected by the feedback are unstable, and further increases in M provide no improvement in the regime of stability.

Figure 11. The lowest eigenfrequency squared as a function of applied voltage V . The gain $A' = 2.05 \times 10^6$ v/m. The solid lines are based on a theory using the coupling of the (1,1), (3,1) and (5,1) modes.

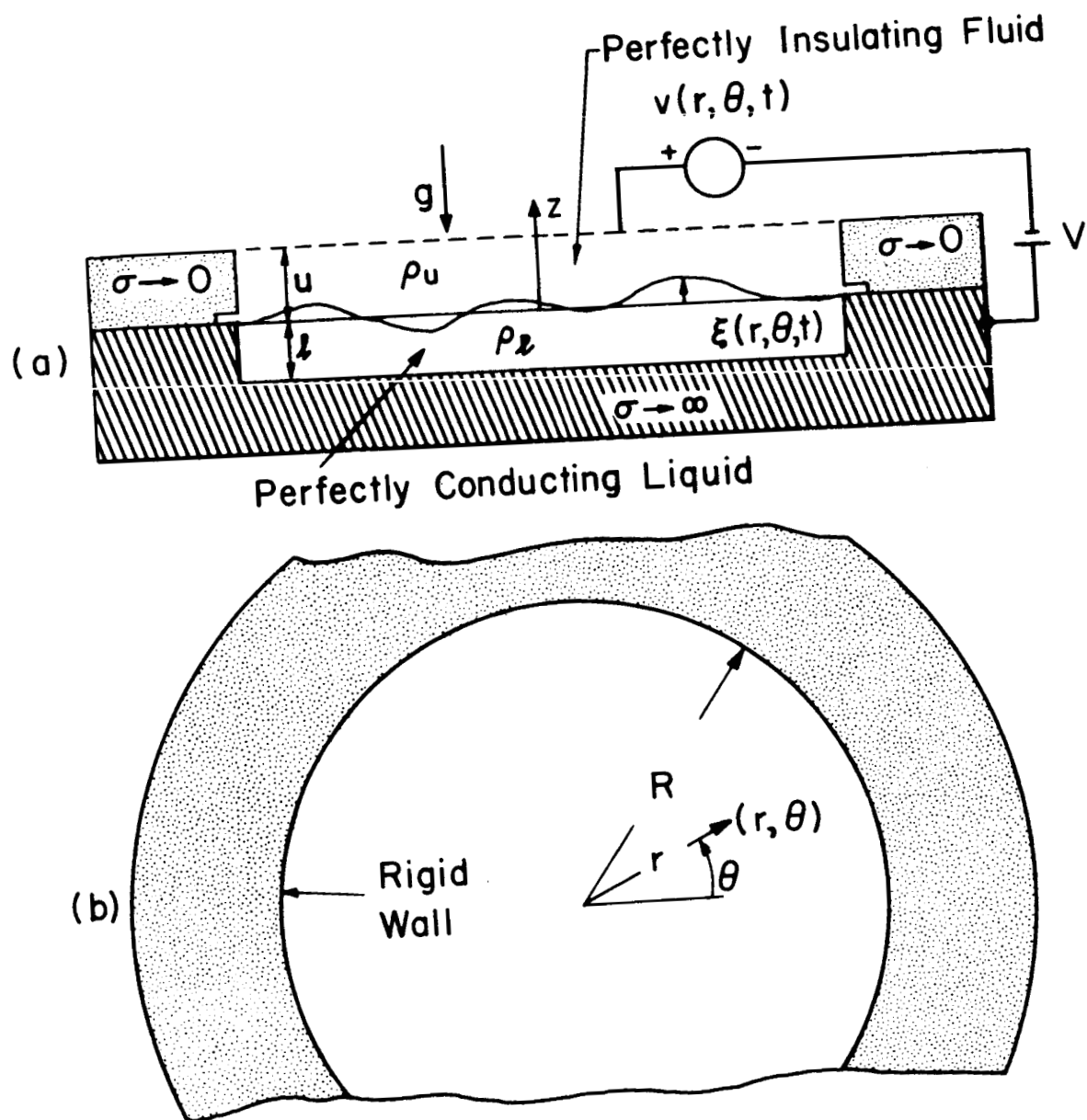


Figure 1. Cross-sectional and top view of electrohydrodynamic resonator. The interface between two liquids is attached at $r = R$ to a rigid wall. The lower liquid is highly conducting and bounded from below by a rigid highly conducting plate, while the upper liquid is insulating and bounded by a rigid surface at the potential $v(r, \theta, t) - V$.

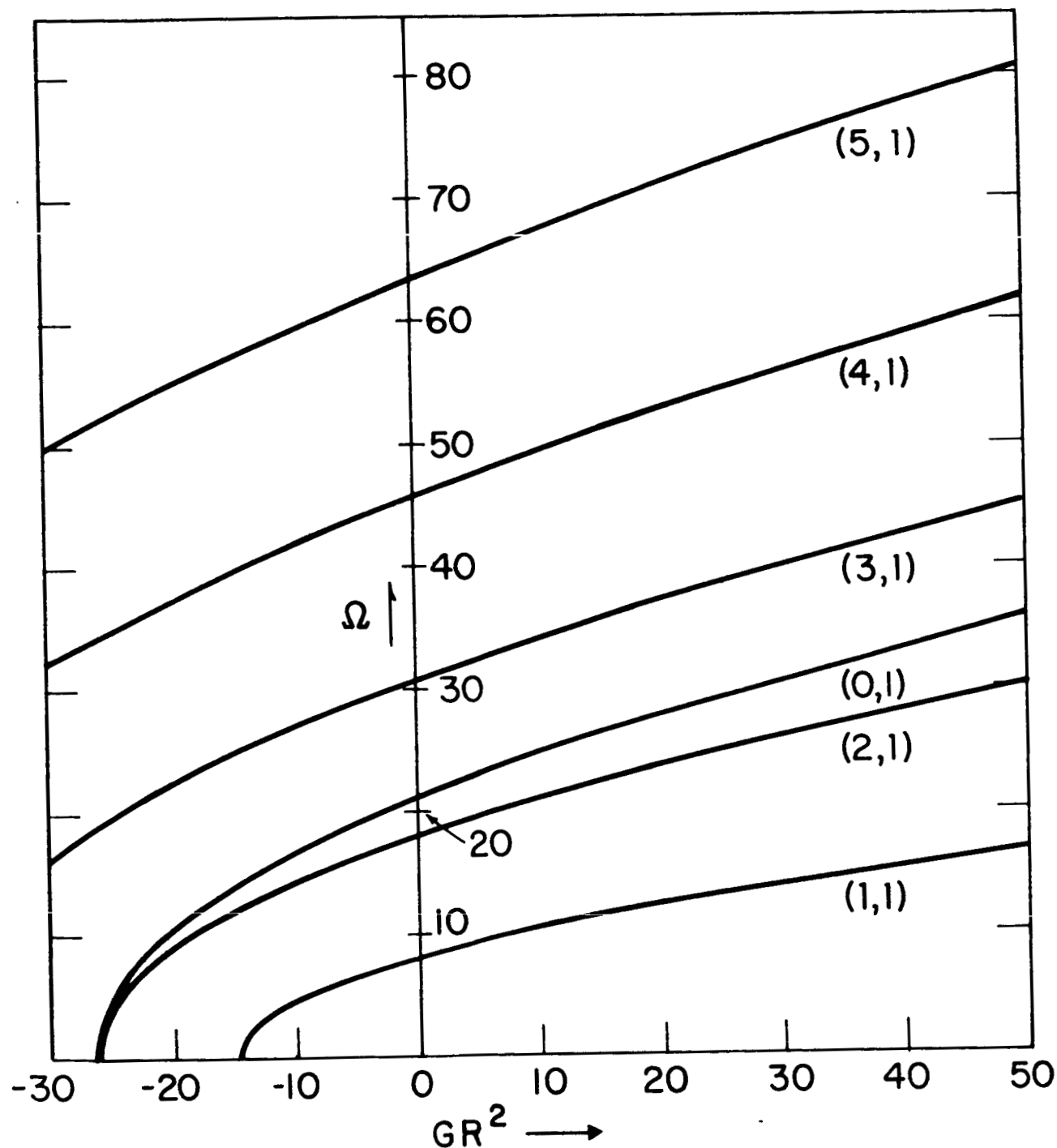


Figure 2. Eigenfrequencies in the absence of feedback for the modes (m,n) . Raising the potential V leads to a decrease in GR^2 which reduces all of the frequencies to the point where they become imaginary and instability impends.

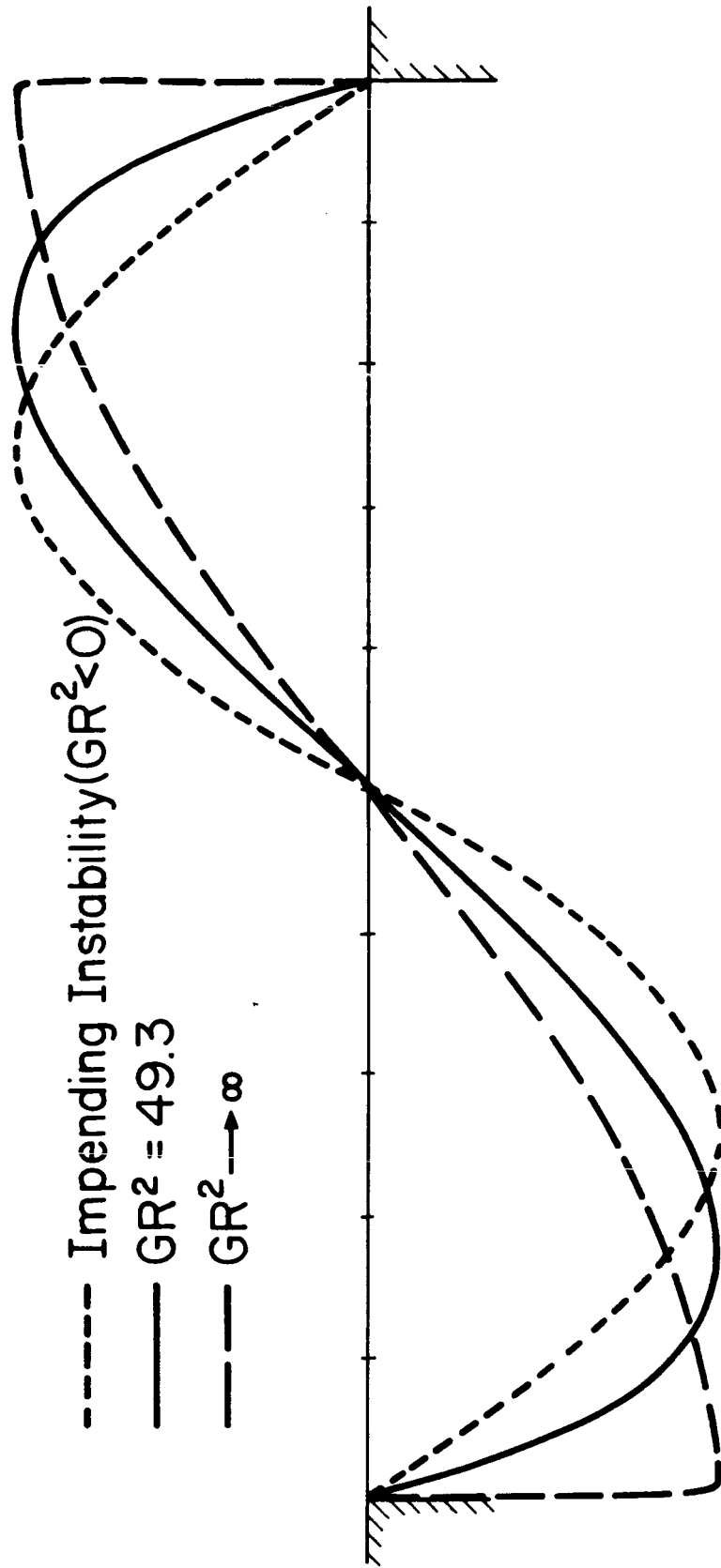


Figure 3. The surface deflection in the (1,1) mode. When GR^2 is very large the eigenfunction approaches that of an ordinary gravity wave. At the point of impending instability ($GR^2 \rightarrow 0$) inertial effects are unimportant and the mode peaks at about a half radius. For an air-water interface and a radius R of about 2 cm, GR^2 is about 50, and the deflections peak midway between the half radius and the outer boundary.

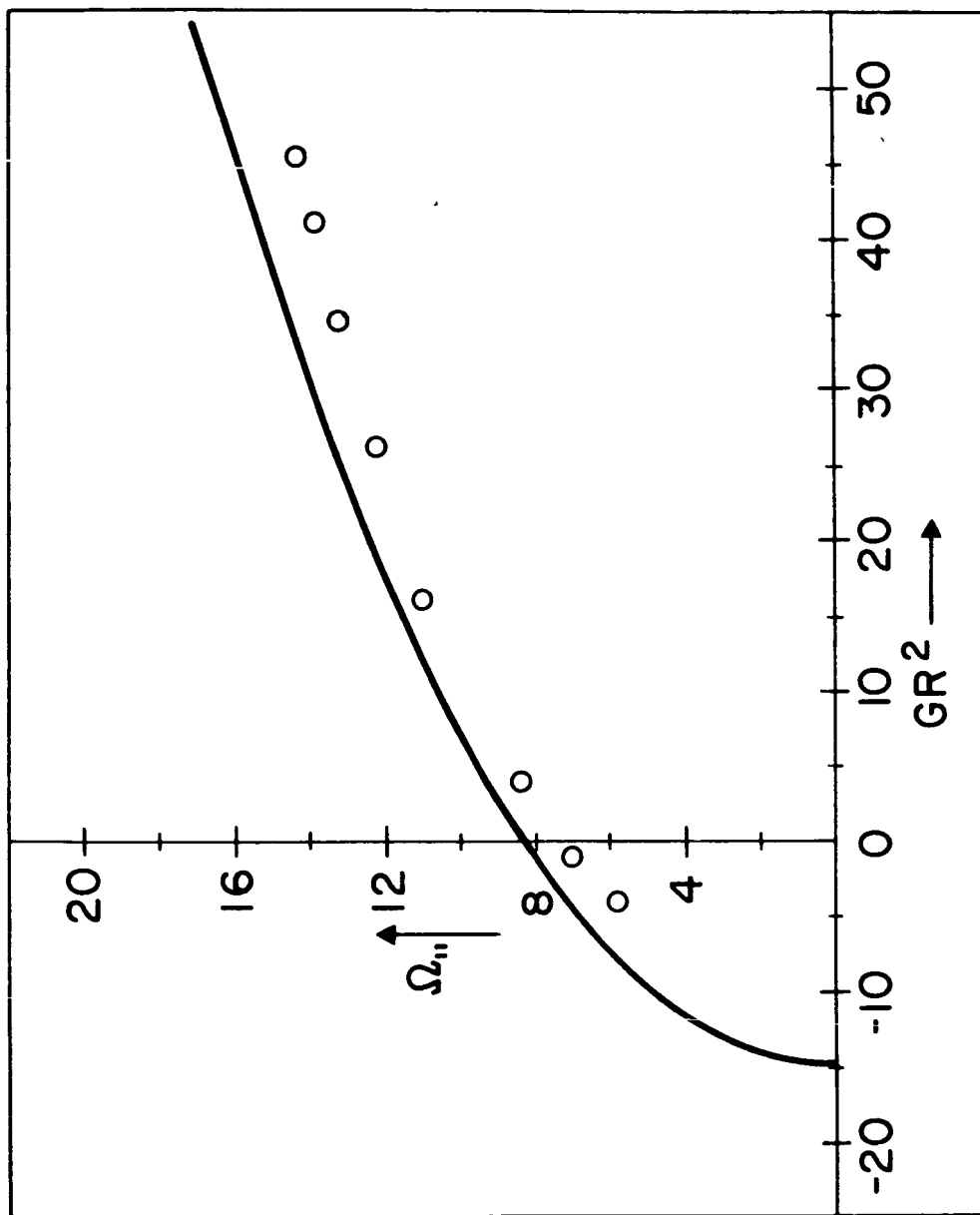


Figure 4. Experimentally measured eigenfrequencies (\circ) as a function of GR^2 (varied by changing the applied voltage V). The solid line is the theoretical result of Section IIIA, $R = 1.9\text{cm}$, $u = 0.785\text{ mm}$, $\ell = 3\text{ mm}$ and the fluids are water and air.

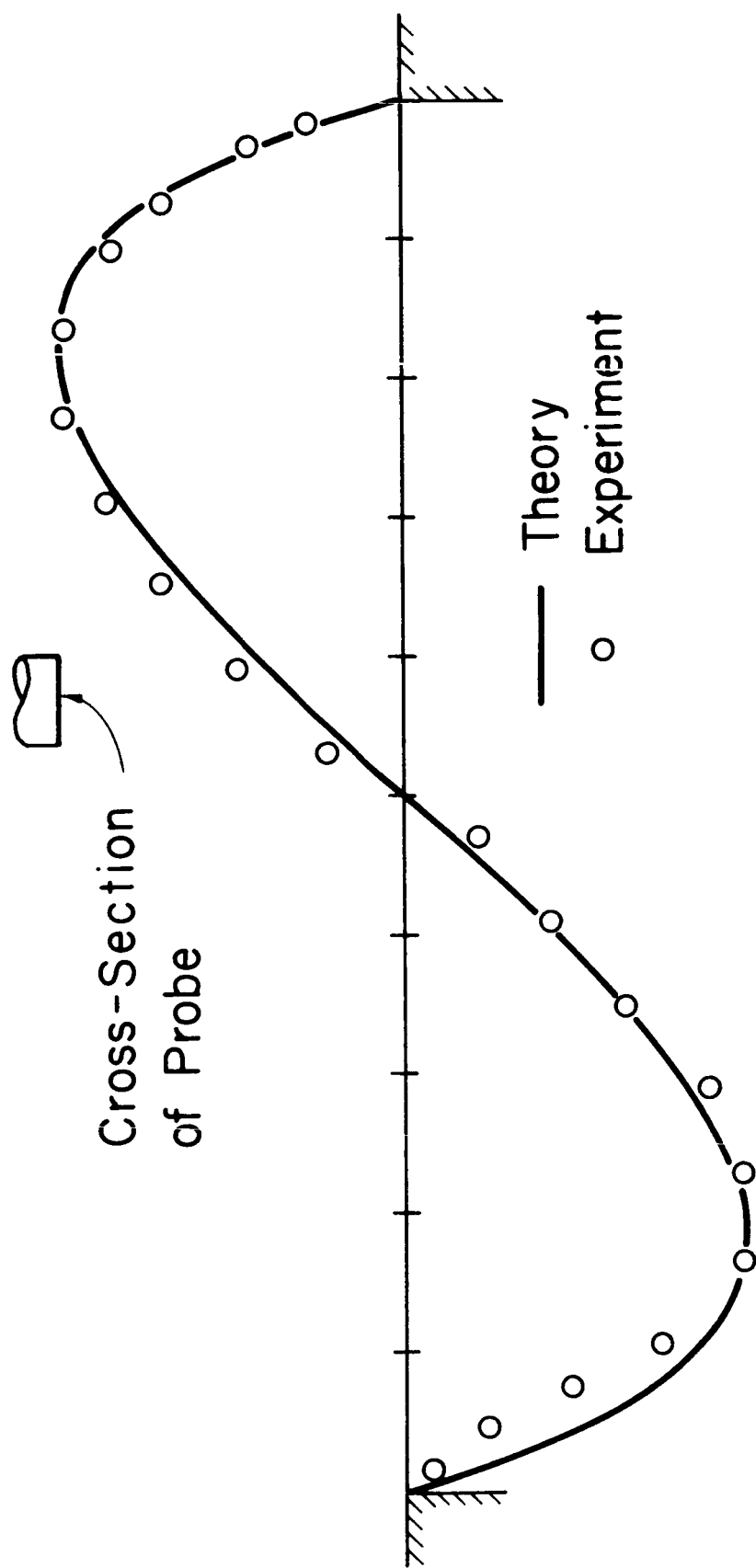


Figure 5. Comparison of theoretical and experimental (1,1) mode eigenfunctions. The experimentally determined deflections represent averages over approximately the probe area. The relative size of the probe is shown.

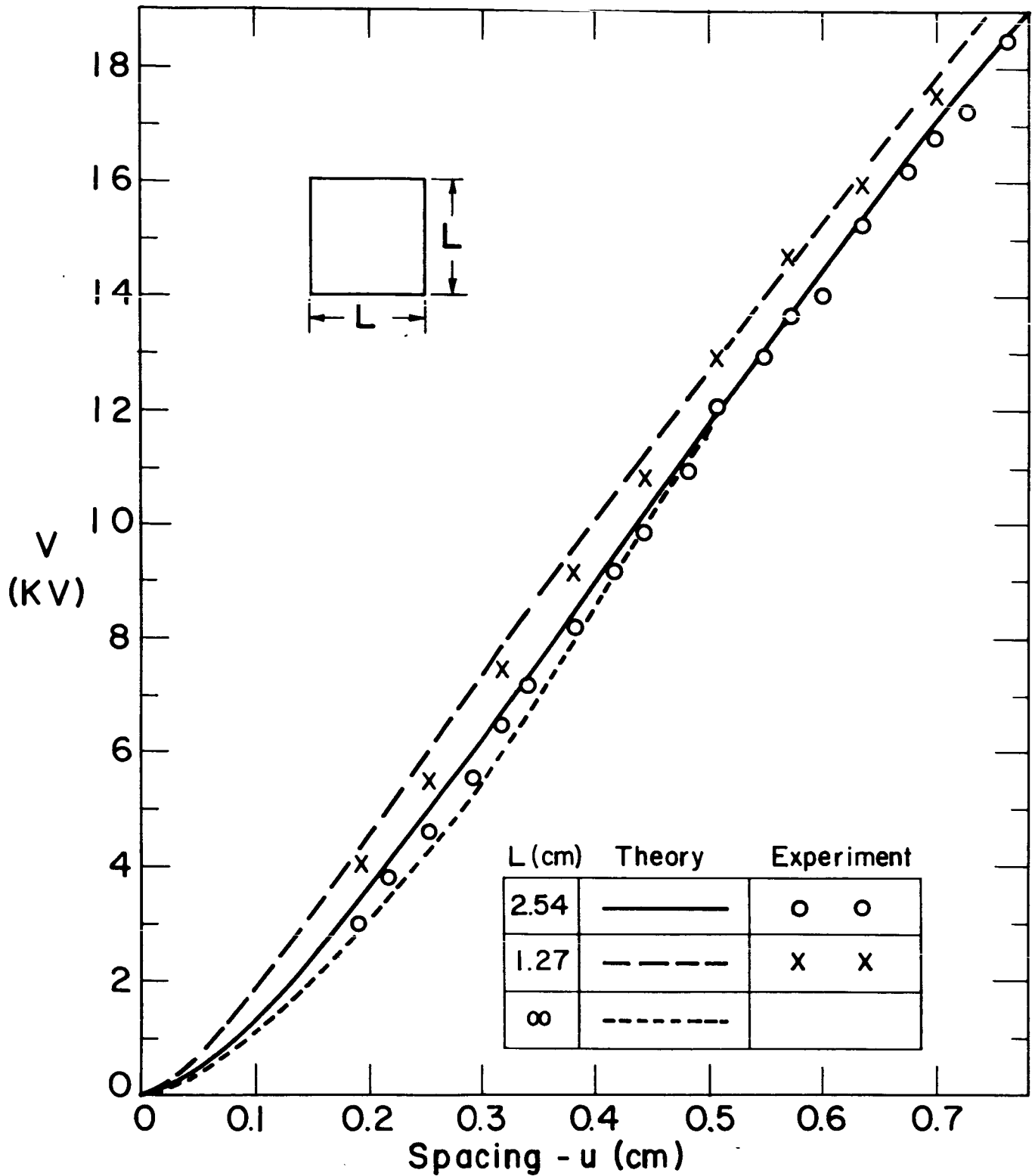


Figure 6. Voltage V for instability as a function of the electrode interface spacing u . The resonator is square, and the three theoretical curves are predicted by Equation (22).

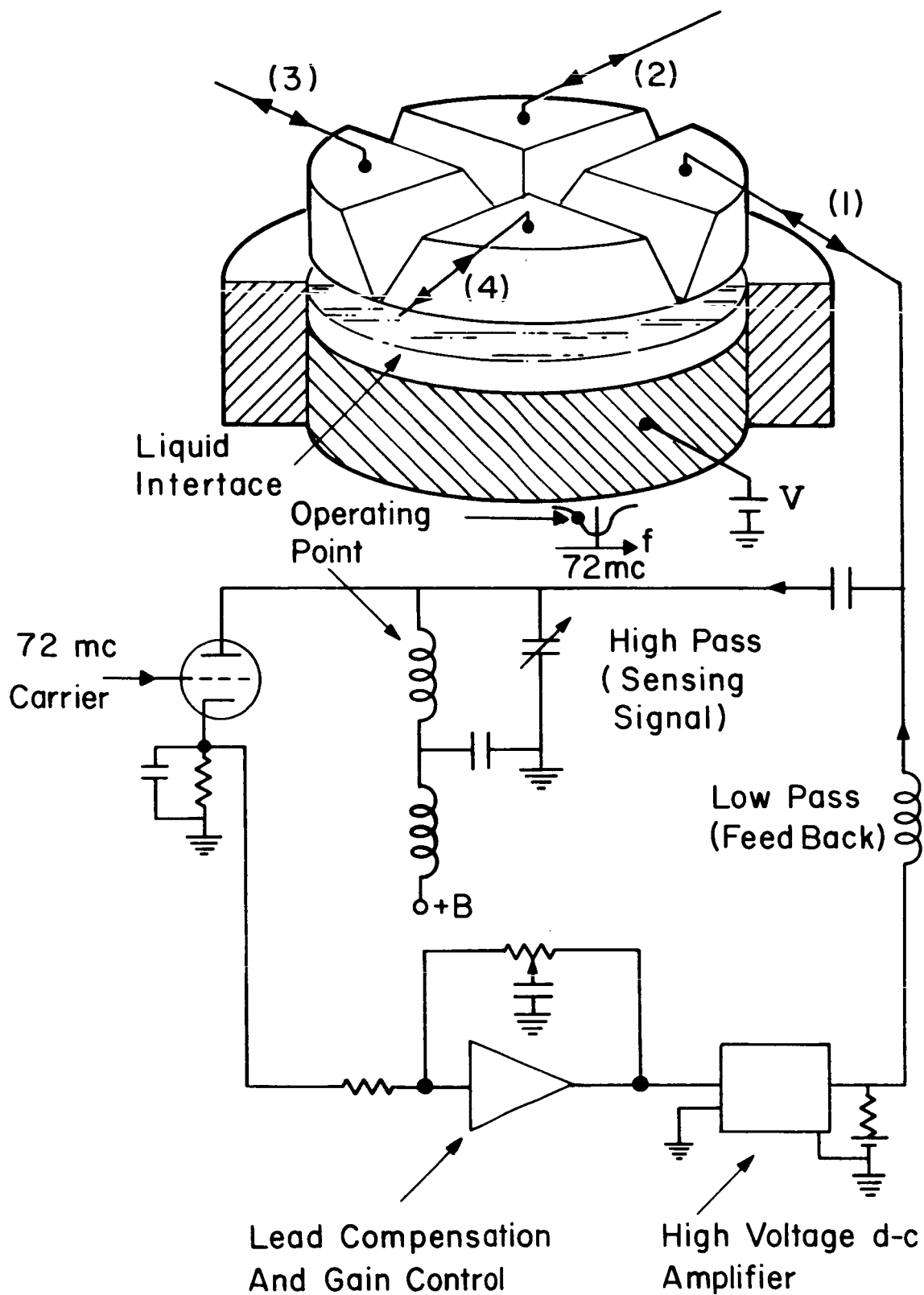


Figure 7. Fluid surface coupled to feedback structure composed of four segments. The sensing and driving circuit for one of the segments is shown.

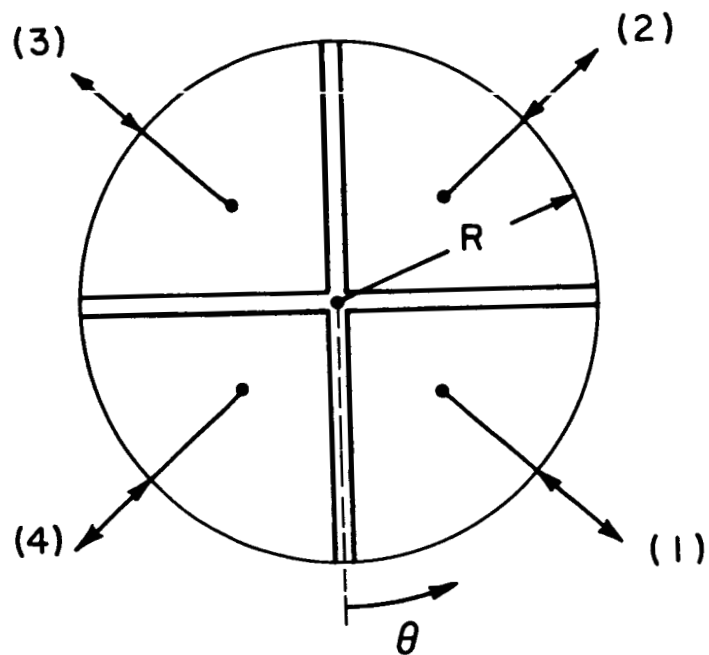


Figure 8. Top view of electrode at $z = u$, showing the four segments with connections to the four feedback loops.

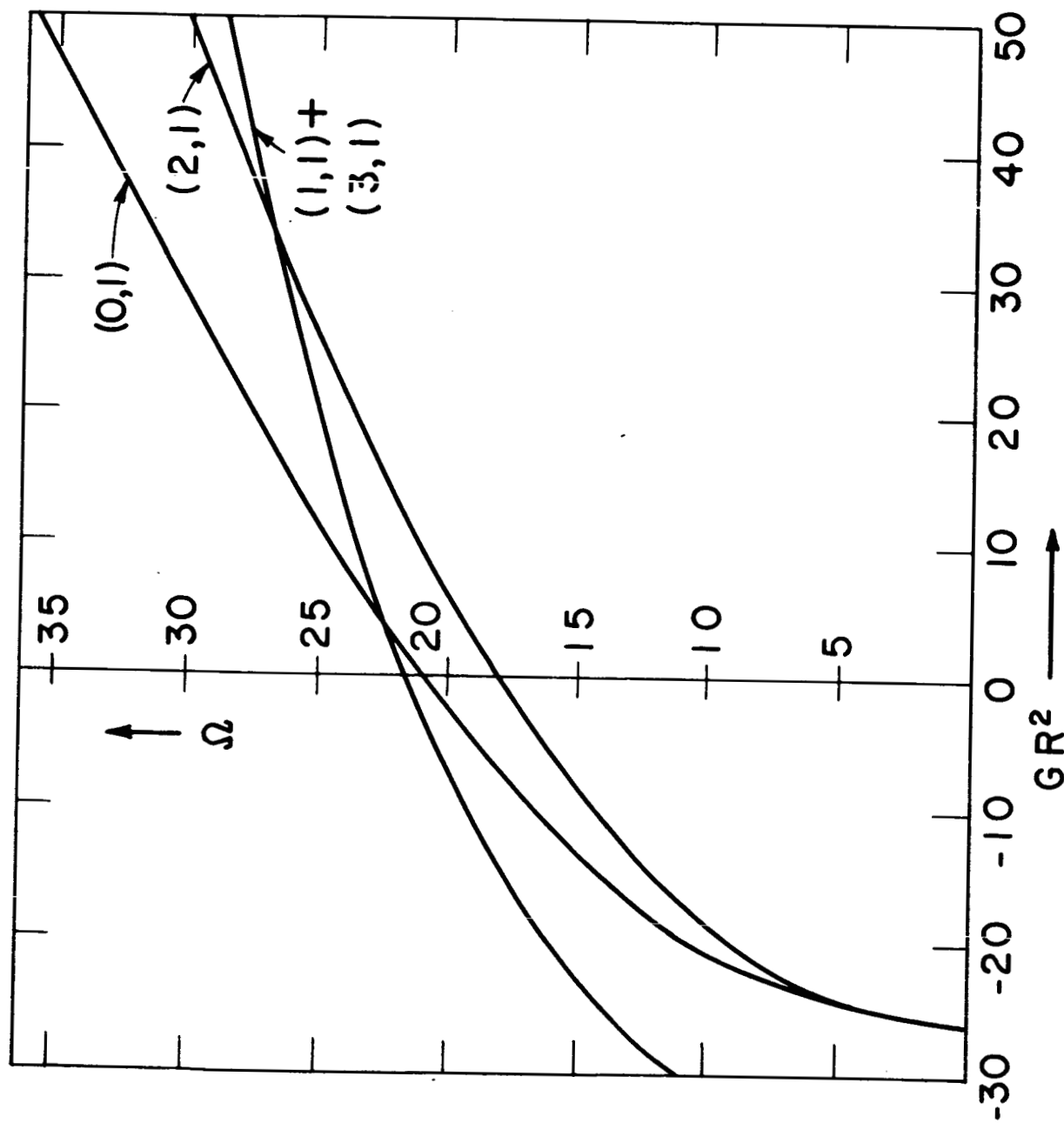


Figure 9. Lowest eigenfrequencies with feedback. Here, $M = 10^3$ which characterizes the magnitude of the feedback gain used in experiments described in Section IVB. The curves are based on the coupling of two modes, and differ very little from those predicted using the coupling of three modes; $(1,1), (3,1)$ and $(5,1)$.

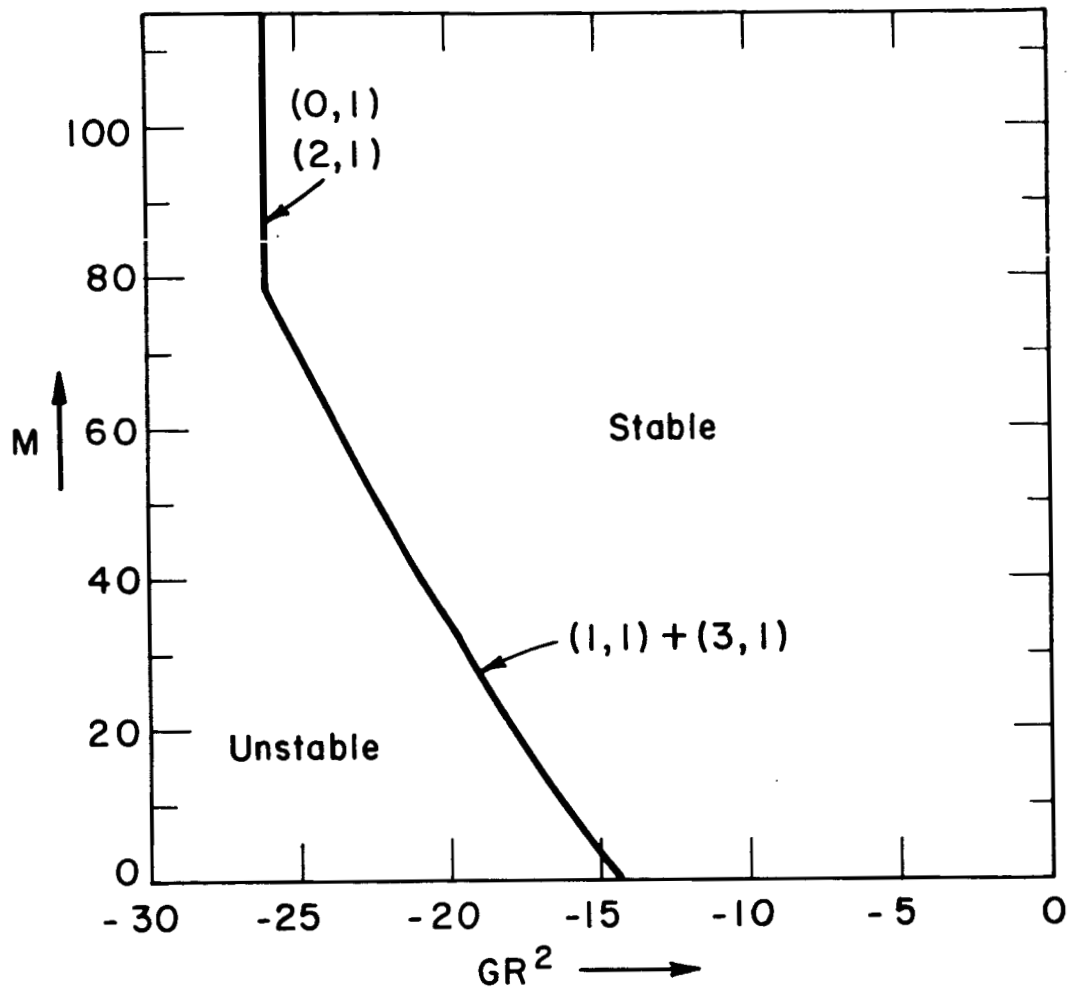


Figure 10. Regime of stability as a function of the feedback M . For small values of M there is an improvement in the electric pressure consistent with stability. Eventually, modes that are unaffected by the feedback are unstable, and further increases in M provide no improvement in the regime of stability.

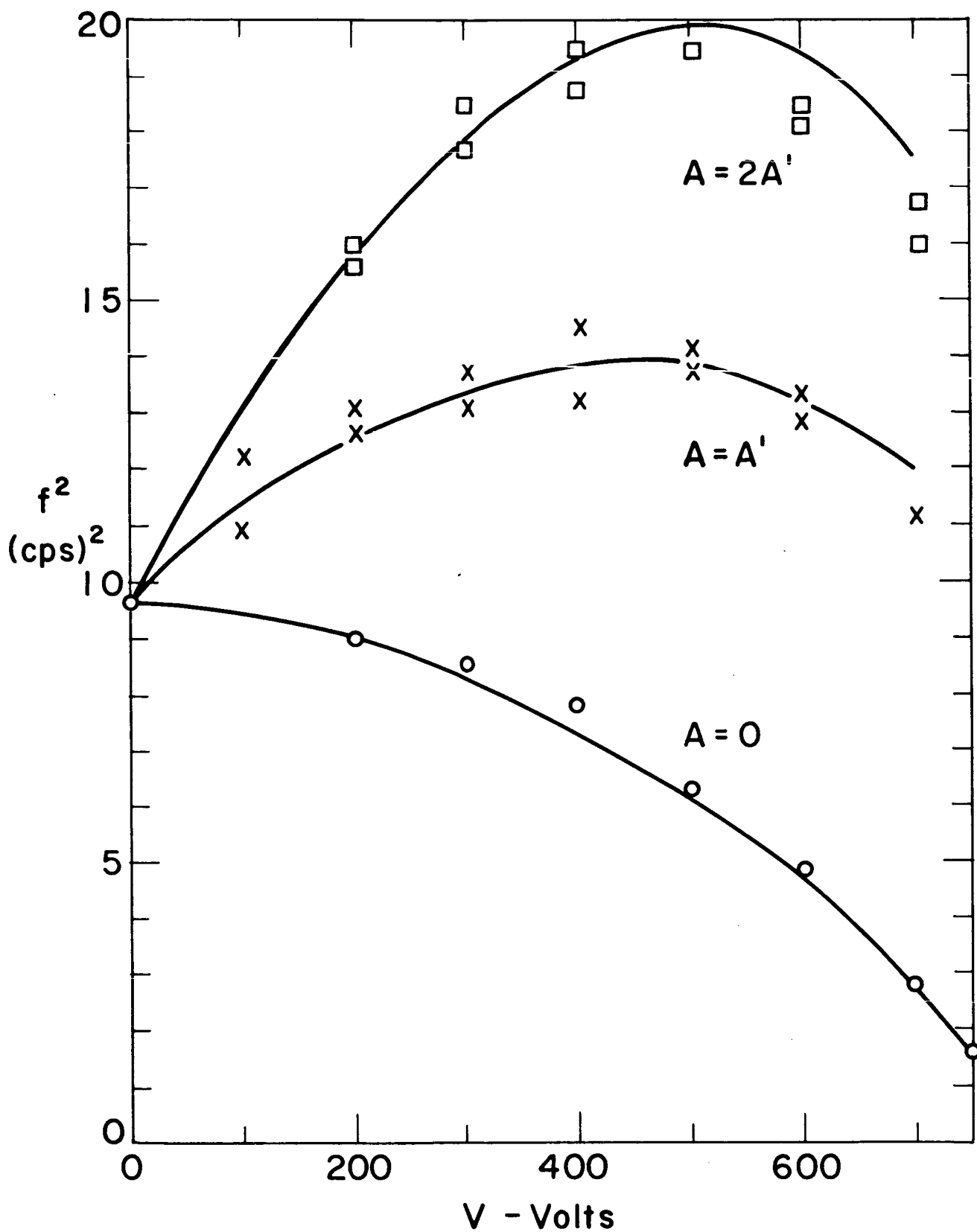


Figure 11. The lowest eigenfrequency squared as a function of applied voltage V . The gain $A' = 2.05 \times 10^6$ v/m. The solid lines are based on a theory using the coupling of the (1,1), (3,1) and (5,1) modes.